# Pseudodielectric function and critical-point energies of iron pyrite

S. G. Choi, J. Hu, L. S. Abdallah, M. Limpinsel, Y. N. Zhang, S. Zollner, R. Q. Wu, and M. Law

Phys. Rev. B **86**, 115207 — Published 12 September 2012

DOI: 10.1103/PhysRevB.86.115207

# Pseudodielectric function and critical point energies of iron pyrite

S.G. Choi,[1,a)] J. Hu,[2] L.S. Abdallah,[3] M. Limpinsel,[4] Y.N. Zhang,[2] S. Zollner,[3] R.Q. Wu,[2] and M. Law[4]

[1]*National Renewable Energy Laboratory, Golden, Colorado 80401, USA*

[2]*Department of Physics and Astronomy, University of California, Irvine, California 92697, USA*

[3]*Department of Physics, New Mexico State University, Las Cruces, New Mexico 88003, USA*

[4]*Department of Chemistry, University of California, Irvine, California 92697, USA*

## ABSTRACT

Spectroscopic ellipsometry was used to determine the pseudodielectric function $\langle\varepsilon\rangle = \langle\varepsilon_1\rangle + i\langle\varepsilon_2\rangle$ spectrum of a natural single crystal of iron pyrite (cubic $FeS_2$) from 0.5 to 4.5 eV with the sample at 77 K. The $\langle\varepsilon\rangle$ spectrum exhibits several pronounced optical features associated with the interband critical points (CPs). Accurate CP energies are obtained by fitting standard lineshapes to second-energy-derivatives of the $\langle\varepsilon\rangle$ data. The electronic origins of the six observed CP features are identified through density functional theory (DFT) calculations and momentum matrix analyses.

[a)] Author to whom correspondence should be addressed. Electronic mail: sukgeun.choi@nrel.gov.

## I. INTRODUCTION

Iron pyrite ($FeS_2$) has long been considered a promising absorber material for thin-film photovoltaics (PVs).[1] Pyrite is reported to possess a bandgap of ~0.95 eV at room temperature, which is suitable for the effective harvesting of solar energy. Its high absorption coefficient ($\alpha > 10^5$ $cm^{-1}$ for $E$ > 1.3 eV) leads to excellent quantum efficiencies (> 90 %) and large photocurrents (> 40 $mA/cm^2$) in single crystals.[2] In addition, the vast abundance and low procurement cost of the constituent elements may make pyrite PV a practical solution for terawatt-scale solar electricity generation.[3]

The complex dielectric function $\varepsilon = \varepsilon_1 + i\varepsilon_2$ and complex refractive index $N = n + ik$ are important for understanding the electronic structure of materials[4] and developing PV device structures.[5] However, only a limited number of $\varepsilon$ and $N$ spectra are available for pyrite from electronic structure calculations[6-9] or optical reflectance measurements.[10-13] Moreover, significant discrepancies exist among the reported spectra and no trustworthy theoretical explanation has been made available so far.

Here, we report the *pseudodielectric function* $\langle\varepsilon\rangle$ spectrum of a natural pyrite single crystal as determined by spectroscopic ellipsometry (SE) at 77 K. SE determines $\varepsilon$ and $N$ spectra without use of the Kramers-Kronig transform and is known to be more accurate than conventional reflectance techniques.[14] Our SE spectrum reveals several above-bandgap optical structures associated with interband critical points (CPs)[15] that correspond to Van Hove singularities in the joint density of states (JDOS) $D_j(E_{cv})$, defined as:

$$D_j(E_{cv}) = \frac{1}{4\pi^3} \int \frac{dS_k}{\left|\nabla_k \left[ E_{cv}(\vec{k}) \right]\right|} \tag{1}$$

Here, $S_k$ is the constant energy surface in reciprocal space defined by $E_{cv}(\vec{k}) \equiv E_c(\vec{k}) - E_v(\vec{k}) = \hbar\omega$. The major optical feature occurs at the CP in reciprocal space where $\left|\nabla_k E_{cv}(\vec{k}) = 0\right|$.

We obtain accurate CP energies by fitting standard lineshapes to second derivatives of the $\langle\varepsilon(E)\rangle$ data[16,17] and identify their electronic origin by comparing the experimental data to the results of density functional theory (DFT) calculations.

## II. EXPERIMENTS

A natural pyrite single crystal from Erzurum, Turkey, sectioned along the (111) surface, was used in this study. For resistivity and Hall effect measurements, ohmic contacts were made to polished slices of the crystal using 40 nm-thick evaporated gold pads covered in dots of colloidal silver paste. The measurements were performed using the van der Pauw method with a magnetic field of 0.55 T and a current of 20 mA. The room-temperature carrier concentration, mobility, and resistivity of this *n*-type crystal were $1 \times 10^{18}$ cm$^{-3}$, 75 cm$^2$/V·s, and 0.083 Ω cm, respectively (Figs. 1c and 1d). These values are typical of relatively highly-doped natural pyrite crystals.

Since SE measurements are often influenced by surface overlayer artifacts such as microscopic roughness, native oxides, and hydrocarbon contamination,[18] we reduced the surface roughness by chemical mechanical polishing of the crystal. After successive grinding steps with abrasive SiC paper and polishing with a diamond particle suspension, the final polishing step employed a colloidal silica suspension with a particle size of 50 nm. Possible silica residue on the surface from the final polishing step was etched away by concentrated hydrofluoric acid (48%) followed by a deionized water rinse. Finally, the crystal was sonicated in methanol. The

resulting root-mean-square roughness was estimated by atomic force microscopy (AFM) to be 2-3 nm over 20 × 20 μm$^2$ areas (Fig. 1b). An X-ray diffraction pattern of a powdered piece of this crystal shows no evidence for any phases other than pyrite (Fig. 1a).

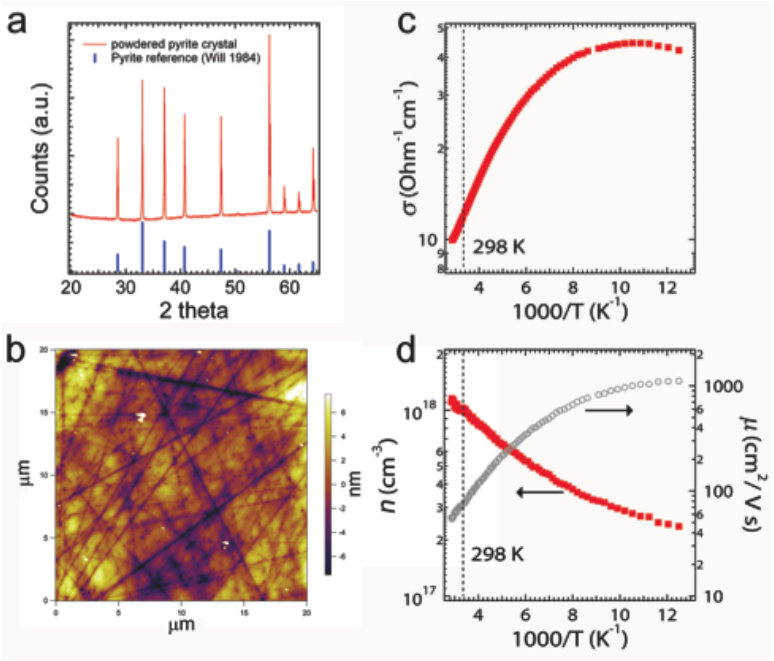


**Figure 1.** (Color online) (a) *X-ray diffraction pattern of a powdered slice of the crystal, showing phase-pure pyrite, along with a pyrite reference pattern.*[19] (b) *AFM topography scan (AC mode), showing a 20 × 20 μm area of the polished crystal with 2.8 nm RMS roughness.* (c) *Temperature-dependent conductivity and* (d) *carrier concentration and mobility from 80 to 350 K determined by Hall effect measurements.*

SE data were acquired from 0.5 to 4.5 eV with a step size was 0.01 eV at 77 K using a rotating-analyzer type ellipsometer equipped with a computer-controlled Berek wave plate compensator (J.A. Woollam Inc., VASE system). The sample temperature was adjusted by a liquid-nitrogen cooled variable-temperature cryostat. The angle of incidence was 70°. To increase the signal-to-noise ratio, each data point was recorded after averaging 100 analyzer cycles (100 revolutions per measurement).

## III. DENSITY FUNCTIONAL PERTURBATION THEORY CALCULATIONS

To elucidate the electronic origin of each CP structure, we carried out spin-polarized density functional calculations with the Vienna *ab initio* simulation package (VASP),[20,21] at the level of the generalized gradient approximation (GGA).[22] The projector augmented wave (PAW) method was adopted for the description of the core-valence interaction.[23,24] The experimental lattice constant ($a$ = 5.418 Å) was used in this work, which is nonetheless very close to the optimized lattice size ($a$ = 5.403 Å). We set an energy cutoff of 350 eV for the basis expansion and used a 13×13×13 $k$-grid mesh to sample the Brillouin zone.[25] The pyrite $FeS_2$ structure is similar to rock salt ($Pa\bar{3}$ space group)[26] and features interpenetrating face-centered cubic sublattices of $Fe^{2+}$ ions and $S_2^{2-}$ dimers pointed along the <111> directions. Each Fe atom has an octahedral coordination to six S atoms, and each S atom has three Fe neighbors and one S neighbor. The octahedral crystal field causes splitting of the 3$d$ orbitals of Fe atom into two groups, $t_{2g}$ ($d_{xy}$, $d_{xz}$ and $d_{yz}$) and $e_g$ ($d_{z^2}$ and $d_{x^2-y^2}$), which constitute the valence and conduction bands, respectively.[8,27] Three $t_{2g}$ states are fully occupied by six 3$d$ electrons of $Fe^{2+}$ cations, which results in a nonmagnetic ground state of pyrite $FeS_2$.[28] On the other hand, the conduction bands are mixtures of Fe-$e_g$ and S-$pp\sigma$* states, so they also comprise $l$ = 1 components around the Fe atoms, which is crucial for efficient optical absorption.

Within the electric dipole approximation, $\varepsilon$(E) can be directly calculated using density functional perturbation theory[29] as (in atomic units):

$$\varepsilon_{xx}(E) = 1 + \frac{4\pi}{\Omega E} \sum_{\vec{k}} \sum_{mn} \frac{f_m - f_n}{E_{mn}} \cdot \frac{\left| p_{x,mn}(\vec{k}) \right|^2}{E - E_{mn} + i\delta}. \quad (2)$$

Here, $\Omega$ is the volume of the pyrite cell, $\delta$ is a broadening width ($\delta$ = 0.1 eV in the present work), $E$ is the incident photon energy, $\vec{k}$ is the wave vector in the Brillouin zone (BZ), $f_m$ is the

electron occupancy of the $m$-th eigenstate, $E_{mn}$ is the energy difference between the $m$-th and $n$-th states and $p_{x,nm}$ is the matrix element of the $x$ component of momentum operator. For a cubic crystal such as pyrite, we have $\varepsilon_{xx} = \varepsilon_{yy} = \varepsilon_{zz} = \varepsilon$.

## IV. RESULTS AND DISCUSSION

The SE-determined $\langle\varepsilon\rangle$ spectrum of the natural pyrite crystal and the calculated $\varepsilon$ curve are shown in Fig. 2. Two prominent CP features are evident in the SE data at ~2.0 eV and ~4.0 eV, as also observed in early studies.[8-13] Although the calculations slightly overestimate the CP energies below 3 eV and underestimate those above it, the overall agreement between experimental and theoretical results is obvious. All six of the major CP features observed experimentally are captured in the DFT calculations. The calculated value of the static dielectric constant ($\varepsilon_\infty = 21$) is also consistent with the experimental data. Although noticeable differences in peak height ratios still exist due to the omission of high level many-body corrections such as GW[30] and time-dependent density functional theory,[31] the present GGA level calculations appear to be adequate for assigning the electronic origins of the optical features.

Although the bandgap energy of pyrite is thought to be ~0.95 eV,[1,2] our SE data show nonzero $\langle\varepsilon_2\rangle$ values below the bandgap rather than an abrupt fundamental absorption edge. This is probably due in part to lifetime broadening and also the presence of native oxides on the crystal surface as well as the nanometer-scale surface roughness.[18] Lifetime broadening due to lattice vibrations causes absorption below the bandgap, which is similar to band tails in amorphous semiconductors.[17] Oxidation of pyrite surfaces can be very rapid[32] and the formation of surface oxides was inevitable during sample preparation. Since the exact thickness and chemical characteristics of native oxides on pyrite are not known *a priori*, we did not attempt a

multilayer analysis in this study. A multilayer analysis with very limited information potentially leads to inaccurate results. Another possible cause of the nonzero absorption below 0.95 eV includes surface and bulk defects that may induce states within the bandgap.[33]

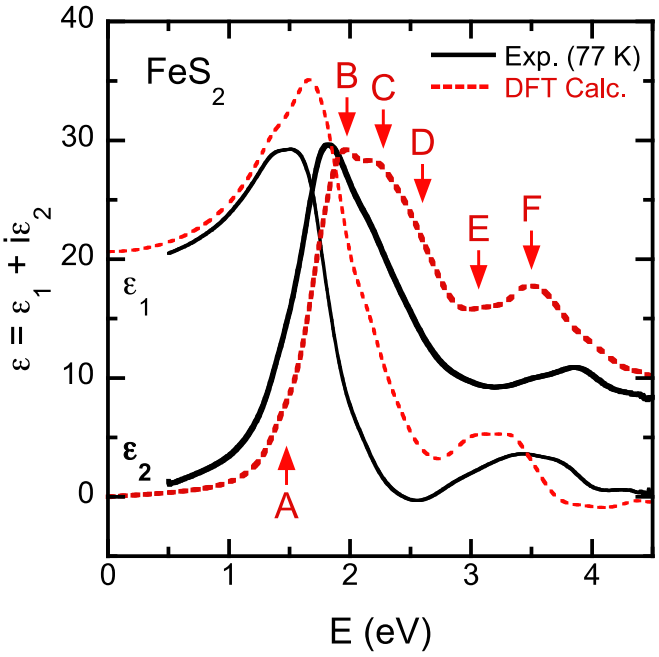


**FIGURE 2.** (Color online) *Experimental (solid black lines) and calculated (dashed red lines) $\varepsilon$ spectra for a pyrite crystal. The experimental data were taken at 77 K. The major CP features seen in the calculated $\varepsilon_2$ spectrum are labeled alphabetically.*

The energies of the CP features observed in our SE data are accurately obtained by fitting the standard analytic CP expressions[34,35] to second-energy-derivatives of the $\langle\varepsilon\rangle$ data calculated numerically from linear filtering algorithms of the Savitzky-Golay type.[36] The CP expressions are:

$$\frac{d^2\varepsilon}{dE^2} = \begin{cases} n(n-1)Ae^{i\phi}(E - E_g + i\Gamma)^{n-2}, n \neq 0 \\ Ae^{i\phi}(E - E_g + i\Gamma)^{-2}, n = 0 \end{cases} \quad (3)$$

where $A$ is the amplitude, $E_g$ is the threshold energy, $\Gamma$ is the broadening parameter, and $\phi$ is the phase. The exponent $n$ has values of -1, -½, 0, and ½ for excitonic, one-, two-, and three-dimensional lineshapes, respectively. The real and imaginary parts were fit simultaneously.

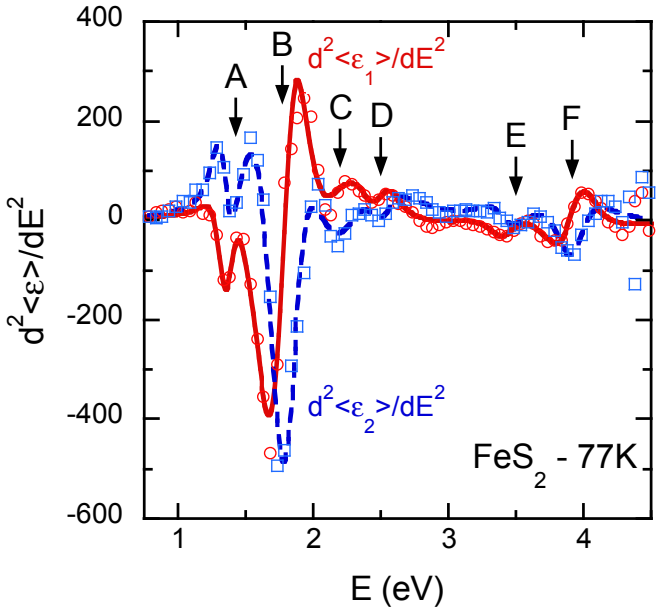


**FIGURE 3.** (Color online) *Best fits to the second derivatives of $<\varepsilon_1>$ (solid red line) and $<\varepsilon_2>$ (dashed blue line). The red circles and blue squares are numerical calculations of $d^2<\varepsilon_1>/dE^2$ and $d^2<\varepsilon_2>/dE^2$, respectively. For clarity, only one fifth of the data points are shown. The lineshapes used to fit the data are labeled in accordance with Fig. 2.*

The $d^2<\varepsilon>/dE^2$ spectrum together with the best-fit curves are shown as open symbols and lines, respectively, in Fig. 3. A total of six excitonic ($n$ = -1) lineshapes[4,17,37-39] are used to fit the data from 1 to 4.5 eV, which resulted in the lowest mean-square deviation. Each peak is identified in accordance with Fig. 2. Several weak CPs (A, C, D and E), clearly resolved in the derivative spectrum, have not been previously discussed in the literature.[6-13] The fit-determined CP energies are listed in Table I. The energy values reported in previous studies[6-9,11,12] as well as our DFT results (discussed below) are also included for comparison. The broadening parameters

Γ for the A, B, C, D, E, and F CPs, obtained by the lineshape analysis, are 131, 255, 542, 184, 239, and 248 meV, respectively. However, one needs to be cautious to interpret these broadening parameters and lineshapes, due to the complexities of band structures of pyrite.

It is known that the optical absorption spectrum of pyrite results from electric dipolar transitions from the Fe $t_{2g}$ states in the valence bands to the Fe $e_g$ and S-S ppσ* mixtures in the conduction bands.[8,27] However, the key states related to these transitions and their distribution in the BZ have not been clearly identified. According to Eq. (2), contributions to $\varepsilon$ from states $m$ and $n$ depend on the square of the momentum matrix element $\left|p_{x,mn}(\vec{k})\right|^2$ and their energy difference $E_{mn}$. By analyzing this matrix element in a narrow energy window over the entire BZ, we can identify the initial and final electronic states across which the electric dipole transitions contribute the most to each CP. Results of these analyses are displayed in Figs. 4(a) and 4(b), along with the calculated band structure of pyrite.

First, it is interesting to note that the magnitude of $\left|p_{x,mn}(\vec{k})\right|^2$ for optical transitions from valence bands (VBs) to the conduction band minimum (CBM) near the center of BZ is negligible, since CBM associates rather purely with S-ppσ* orbitals whereas VB states mostly localize around the Fe atoms. As a result, the optical absorption edge of iron pyrite starts much higher than the band gap. The main absorption features, i.e., the "B" CP at 2.0 eV and the "C" CP at 2.3 eV in the calculated $\varepsilon_2$ curve (dashed red) in Fig. 2, originate from transitions between orbital of Fe atoms. To better appreciate this, we plot in Fig. 4(b) the isosurface of $\left|p_{x,mn}(\vec{k})\right|^2$ in the BZ and its two-dimensional contour map at $k_z = \pi/a$ for the "B" CP with $E_{mn} = 2.0 \pm 0.1$ eV. Clearly, the main contributions to the "B" CP are from electric dipole transitions in the vicinity of the M points in the BZ. The initial and final states that are responsible for the "B" CP are the

occupied Fe $t_{2g}$ state and hybridized Fe $e_g$ and S-S ppσ* state as depicted in Fig. 4(a). The "C" CP can be assigned to transitions near the X point, along with a relatively weak transition at the M point, as shown Fig. 4(a). We note that the "C" CP and its origin have not been identified in previous theoretical studies.[6-9]

This procedure was applied to all CPs, and arrows in Fig. 4(a) show the key pairs of states and their locations in the BZ. The second major CP feature "F" from DFT lies at ~3.5 eV, which is ~0.3 eV lower than the corresponding experimental value. The transitions associated with this CP occur near the M, Γ, and R points in the BZ, with both the initial and final states a mixture of Fe 3*d* and S 3*p* orbitals. Our momentum matrix analyses suggest that the transition occurring near the M point is the dominant contribution to "F". Our assignments for the "B" and "F" CPs are similar to those of Lauer *et al*.[6] and Antonov *et al*.[8]

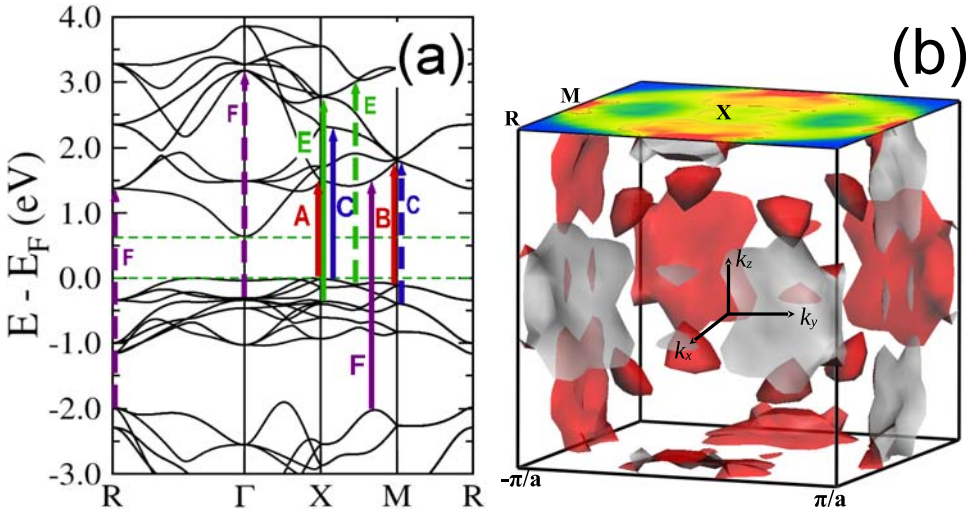


**FIGURE 4.** (Color online) *(a) Band structure of bulk pyrite, with arrows denoting the main transitions associated with the CPs labeled in Fig. 2. (b) The isosurface of* $\left|p_{x,mn}(\bar{k})\right|^2$ *in the Brillouin zone for the "B" CP. A two-dimensional contour is also shown for* $k_z = \pi/a$ *(a is the lattice constant of pyrite).*

We note that different explanations for the origin of features "B" and "F" have been reported. Based on the results from their full-potential linearized augmented plane wave calculations, Vadkhiya *et al*.[9] assigned the "B" and "F" CPs to the transitions from Fe 3*d* to S 3*p* states at the R point and X point, respectively. However, in our calculation, the momentum matrices related these transitions are almost zero, due to the very small overlap between the Fe $t_{2g}$ and S $pp\sigma^*$ orbitals. Schlegel *et al*.[11] related the structure at ~2 eV ("B" CP) to 3*d intraband* transitions from $t_{2g}$ states to antibonding $e_g$* states, and the high-energy structures ("F" CP) to *interband* transitions from states of largely S 3*p* character into Fe $e_g$* states. These assignments appear to be arbitrary and do not agree with our results in Fig. 4(a).

Among the minor peaks that have not been discussed in previous studies,[6-13] the "A" CP at ~1.5 eV is crucial for applications of pyrite in PV since it is the first major absorption feature above the bandgap. It results from the transition between the Fe $t_{2g}$ state at the valence band maximum and the mixed Fe-S state (Fe-$e_g$ + S-pp$\sigma$*) near the X point. The *plateau-like* "E" CP at ~3 eV is composed of a series of transitions from the Fe $t_{2g}$ states to hybridized states of Fe $e_g$ and S-pp$\sigma$* along the X-M direction in the BZ. Finally, the "D" CP results mainly from transitions in the wide region near the M points, and contributions from other *k*-points are also substantial. Therefore, we chose not to denote the transitions responsible for this CP in Fig. 4(a).

Finally, we want to point out that most CPs, in particular the C and E CPs, contain multiple contributions from different parts of BZ. This makes the assignments of dimensionality and type of symmetry of their corresponding Van Hove singularities impractical. Nevertheless, we may still roughly trace their origins from the band structure in Fig. 4. For example, the B CP shows two-dimensional saddle-point feature in the MRM plane, whereas the F CP appears to be a three-dimensional $M_0$ singularity.

In order to obtain the better band gap, the Hubbard correction was typically included in recent density functional calculations for iron pyrite (e.g., U = 2.0 eV for the Fe 3*d* orbitals).[27] We found, however, that it significantly worsens the agreement of optical spectrum by shifting most CPs upward by 0.3-0.5 eV. On the other hand, the GW correction reduces the band gap to 0.4 eV but does not much affect the optical functions. Also, unreasonably large band gap, 2.70 eV, was obtained using hybrid functional (HSE06). It is still unknown how to best invoke the correction of the correlation effect for pyrite. Since the local-field and excitonic effects were also omitted in the present calculations, there are rooms for further studies to achieve better quantitative comparison for positions and intensity ratios of CPs.

## IV. CONCLUSIONS

The pseudodielectric function $\langle\varepsilon\rangle$ of a natural iron pyrite single crystal has been determined by spectroscopic ellipsometry at 77 K. Our $\langle\varepsilon\rangle$ data show a total of six interband critical points (CPs). The CP energies were obtained by the standard lineshape analysis and their electronic origins were identified by DFT calculations and momentum matrix analyses. Our results help to better understand the electronic structure and related optical properties of iron pyrite, which will in turn aid in the development of high-performance pyrite solar cells.

**ACKNOWLEDGMENTS**

This work was supported by the U.S. Department of Energy (DOE) under Contract No. DE-AC36-08-GO28308. Work at New Mexico State University was supported by the National Science Foundation (NSF) Grant No. DMR-1104934. J. H., Y. N. Z., and R. Q. W. were supported by the NSF Solar Program (Award No. CHE-1035218). M. L. and M. L. acknowledge support from the U.S. DOE under Contract No. DE-EE0005324, funded by the SunShot Next Generation Photovoltaics II (NextGen PVII) program. The authors thank Dr. Andre Puschnig and Naturhistorisches Museum Basel for providing the pyrite crystal, catalog number 18249.

**TABLE I.** CP energies (in eV) for pyrite. Previously reported CP energies are included for comparison.

| CP | | A | B | C | D | E | F |
|---|---|---|---|---|---|---|---|
| This work | Exp | 1.36 | 1.78 | 2.09 | 2.49 | 3.41 | 3.92 |
| | Theory | 1.30 | 1.96 | 2.27 | 2.60 | 3.10 | 3.50 |
| Ref. 6 | | | 2.00 | | | | |
| Ref. 7 | | | 2.10 | | | | 3.30 |
| Ref. 8 | | | 2.10 | | | | 3.50 |
| Ref. 9 | | | 2.00 | | | | 3.60 |
| Ref. 11 | | | 1.70 | | 2.30 | | 3.80 |
| Ref. 12 | | | 1.6 | | | | 4 |

## REFERENCES


[1] A. Ennaoui, S. Fiechter, Ch. Pettenkofer, N. Alonso-Vante, K. Büker, M. Bronold, Ch. Höpfner, and H. Tributsch, Solar Energy Materials and Solar Cells **29**, 289 (1993).

[2] J. Puthussery, S. Seefeld, N. Berry, M. Gibbs, and M. Law, J. Am. Chem. Soc. **133**, 716 (2011).

[3] C. Wadia, A.P. Alivisatos, and D.M. Kammen, Environ. Sci. Technol. **43**, 2072 (2009).

[4] S.G. Choi, M. van Schilfgaarde, D.E. Aspnes, A.G. Norman, J.M. Olson, T.J. Peshek, and D.H. Levi, Phys. Rev. B **83**, 235210 (2011).

[5] O.E. Semonin, J.M. Luther, S. Choi, H.-Y. Chen, J. Gao, A.J. Nozik, and M.C. Beard, Science **334**, 1530 (2011).

[6] S. Lauer, A.X. Trautwein, and F.E. Harris, Phys. Rev. B **29**, 6774 (1984).

[7] G.U. von Oertzen, R.T. Jones, and A.R. Gerson, Phys. Chem. Minerals **32**, 255 (2005).

[8] V.N. Antonov, L.P. Germash, A.P. Shpak, and A.N. Yaresko, Phys. Status Solidi B **246**, 411 (2009).

[9] L. Vadkhiya and B.L. Ahuja, J. Alloys Compounds **509**, 3042 (2011).

[10] T.A. Bither, R.J. Bouchard, W.H. Cloud, P.C. Donohue, and W.J. Siemons, Inorganic Chem. **7**, 2208 (1968).

[11] A. Schlegel and P. Wachter, J. Phys. C **9**, 3363 (1976).

[12] S. Suga, K. Inoue, M. Taniguchi, S. Shin, M. Seki, K. Sato, and T. Teranishi, J. Phys. Soc. Jpn. **52**, 1848 (1983).

[13] I.J. Ferrer, D.M. Nevskaia, C. de las Heras, C. Sánchez, Solid State Commun. **74**, 913 (1990).

[14] D.E. Aspnes, in *Handbook of Optical Constants of Solids*, edited by E.D. Palik (Academic, Orlando, 1985), Vol. I, p. 89.

[15] M.L. Cohen and J.R. Chelikowsky, *Electronic structure and optical properties of semiconductors*, 2nd Edition (Springer-Verlag, Berlin, 1989).

[16] L. Viña, C. Umbach, M. Cardona, and L. Vodopyanov, Phys. Rev. B **29**, 6752 (1984).

[17] L. Viña, S. Logothetidis, and M. Cardona, Phys. Rev. B **30**, 1979 (1984).

[18] D.E. Aspnes and A.A. Studna, Appl. Phys. Lett. **39**, 316 (1981).

[19] G. Will, J. Lauterjung, H. Schmitz, and E. Hinze, Mater. Res. Soc. Symp. Proc. **22**, 49 (1984).

[20] G. Kresse and J. Furthmuller, Comput. Mater. Sci. **6**, 15 (1996).

[21] G. Kresse and J. Furthmuller, Phys. Rev. B **54**, 11169 (1996).

[22] J. P. Perdew, K. Burke, and M. Ernzerhof, Phys. Rev. Lett. **77**, 3865 (1996).

[23] P. E. Blochl, Phys. Rev. B **50**, 17953 (1994).

[24] G. Kresse and D. Joubert, Phys. Rev. B **59**, 1758 (1999).

[25] H. J. Monkhorst and J. D. Pack, Phys. Rev. B **13**, 5188 (1976).

[26] P. Bayliss, Am. Mineral. **74**, 1168 (1989).

[27] J. Hu, Y. Zhang, M. Law, and R. Wu, Phys. Rev. B **85**, 085203 (2012). In the present study, the U-correction term was omitted to best fit the experimental spectra.

[28] F. Hulliger and E. Mooser, J. Phys. Chem. Solids **26**, 429 (1965).

[29] M. Gajdos, K. Hummer, G. Kresse, J. Furthmuller, and F. Bechstedt, Phys. Rev. B **73**, 045112 (2006).

[30] M. S. Hybertsen and S. G. Louie, Phys. Rev. B **34**, 5390 (1986).

[31] L. Reining, V. Olevano, A. Rubio, and G. Onida, Phys. Rev. Lett. **88**, 066404 (2002).

[32] C.M. Eggleston, J.-J. Ehrhardt, W. Stumm, Am. Mineralogist **82**, 1036 (1996).

[33] Y.N. Zhang, J. Hu, M. Law, and R.Q. Wu, Phys. Rev. B **85**, 085314 (2012).

[34] M. Cardona, *Modulation Spectroscopy, Suppl. 11 of Solid State Physics*, edited by F. Seitz, D. Turnbell, and H. Ehrenreich (Academic, New York, 1969).

[35] D.E. Aspnes, in *Handbook of Semiconductors*, edited by M. Balkanski (North-Holland, Amsterdam, 1980), Vol. 2, p. 109.

[36] A. Savitzky and M.J.E. Golay, Anal. Chem. **36**, 1627 (1964).

[37] S. Adachi and T. Taguchi, Phys. Rev. B **43**, 9569 (1991).

[38] Y.D. Kim, S.L. Cooper, M.V. Klein, and B.T. Jonker, Phys. Rev. B **49**, 1732 (1994).

[39] P. Lautenschlager, M. Garriga, L. Viña, and M. Cardona, Phys. Rev. B **36**, 4821 (1987).